Impacts of Adjacent Pixels on Retrieved Urban Surface Temperature

Feng, Liping; Yang, Jinxin; Zhu, Lili; Ouyang, Xiaoying; Shi, Qian; Xu, Yong; Menenti, Massimo

DOI
10.3390/rs17173077

Publication date
2025

Document Version
Final published version

Published in
Remote Sensing

remote sensing

MDPI

Article

Impacts of Adjacent Pixels on Retrieved Urban Surface Temperature

Liping Feng [1], Jinxin Yang [1,*], Lili Zhu [1], Xiaoying Ouyang [2,3], Qian Shi [4], Yong Xu [1] and Massimo Menenti [5,6]

1 School of Geography and Remote Sensing, Guangzhou University, Guangzhou 510006, China; 32101800015@e.gzhu.edu.cn (L.F.); zhull@e.gzhu.edu.cn (L.Z.); xu1129@gzhu.edu.cn (Y.X.)
2 International Research Center of Big Data for Sustainable Development Goals, Beijing 100094, China; ouyxy@aircas.ac.cn
3 Aerospace Information Research Institute, Chinese Academy of Sciences, Beijing 100094, China
4 School of Geography and Planning, Sun Yat-sen University, Guangzhou 510006, China; shixi5@mail.sysu.edu.cn
5 Institute for Tibetan Plateau Research, Chinese Academy of Sciences, Beijing 100094, China; m.menenti@tudelft.nl
6 Faculty of Civil Engineering and Earth Sciences, Delft University of Technology, 2600 GA Delft, The Netherlands
* Correspondence: yangjx11@gzhu.edu.cn

Abstract

Accurate estimation of urban land surface temperature (ULST) is critical for studying urban heat islands, but complex three-dimensional (3D) structures and materials in urban areas introduce significant adjacency effects into remote sensing retrievals. To investigate the influence of different factors on the adjacency effects, this study employed the DART model to quantify brightness temperature differences (ΔTb) of urban pixels by comparing their simulated radiance in two scenarios: (1) an isolated state (no adjacent buildings) and (2) an adjacent state (with surrounding buildings). ΔTb, representing the adjacency effect, was systematically analyzed across spatial resolutions (1–120 m), building geometry (building height BH, roof area index λ_p, adjacent obstruction degree $SVF_{Obs.}$), and material reflectance (reflectance R = 0.05, 0.1, 0.15) to determine key influencing factors. The results demonstrate that (1) adjacency effects intensify significantly with higher spatial resolution (mean ΔTb ≈ 5 K at 1 m vs. ≈2 K at 30 m), with 60–90 m identified as the critical resolution range where the adjacency-induced error is attenuated to a level (ΔTb < 1 K) that is commensurate with the intrinsic uncertainty of current mainstream ULST algorithms; (2) increased building height, reduced density (λ_p), and greater adjacent obstruction ($SVF_{Obs.}$) exacerbate adjacency effects; (3) material emissivity ($\varepsilon = 1 - R$) is the dominant factor, where low-ε materials (high R) exhibit markedly stronger adjacency effects than geometric influences (e.g., ΔTb at R = 0.15 is approximately three times higher than at R = 0.05); and (4) temperature differences among surface components exert minimal influence on adjacency effects (ΔTb < 0.5 K). This study clarifies key factors driving adjacency effects in high-resolution ULST retrieval and defines the critical spatial resolution for simplifying inversions, providing essential insights for accurate urban temperature estimation.

Keywords: ULST; urban geometry; adjacency effects; DART

Academic Editor: Carmine Serio

Received: 16 July 2025
Revised: 23 August 2025
Accepted: 28 August 2025
Published: 4 September 2025

Citation: Feng, L.; Yang, J.; Zhu, L.; Ouyang, X.; Shi, Q.; Xu, Y.; Menenti, M. Impacts of Adjacent Pixels on Retrieved Urban Surface Temperature. *Remote Sens.* **2025**, *17*, 3077. https://doi.org/10.3390/rs17173077

1. Introduction

Land surface temperature (LST) is a critical variable for understanding physical processes on the Earth's surface [1,2], with wide applications across domains. It is vital for

public health, environmental monitoring studies [3], and urban climate change studies [4]. Rapid urbanization has substantially altered the natural state of the land surface. The proliferation of urban agglomerations and densely packed buildings induces airflow obstruction [5] and increases the probability of multiple scattering, leading to persistently elevated surface temperatures and enhanced outward radiative energy emission. Urban land surface temperature (ULST) is a key indicator of urban sustainability. Accurate estimation of ULST is crucial for understanding the urban heat island (UHI) effect [6,7], managing energy consumption, and assessing human thermal comfort.

Satellite remote sensing is an effective tool for continuous, large-scale monitoring of ULST [8], offering substantial advantages over traditional ground-based measurements in spatial coverage, timeliness, and cost-effectiveness [9]. However, cities—typical heterogeneous landscapes with structural and material differences from natural surfaces—present significant challenges for accurate ULST retrieval from remote sensing data [10]. These challenges stem from urban geometry interfering with radiative transfer processes. Urban geometry not only induces a "cavity effect" through multiple scattering [10] but also makes the thermal radiation contribution from adjacent pixels (i.e., the adjacency effect) a non-negligible source of error [11].

The influence of urban geometry on LST is pronounced. Conventional LST retrieval algorithms (e.g., single-channel methods, split-window algorithms) [12,13] assume surfaces are "flat, homogeneous, and isothermal" [14], which contradicts urban environmental reality and compromises ULST retrieval accuracy. Studies have demonstrated that LST retrieved without considering geometric effects is typically higher than that which accounts for them [10]. This discrepancy arises because multiple scattering and reflections within urban areas (i.e., the cavity effect) elevate the effective emissivity above the inherent material emissivity, leading to temperature differences. Yang [10] proposed the UEM-SCM method, which quantifies geometric influences via a radiative transfer model that incorporates the sky view factor (SVF) into a split-window algorithm, thereby distinguishing geometric effects from atmospheric effects. This study found that the uncorrected split-window algorithm misattributes part of the geometric contribution to atmospheric effects, resulting in biases of up to 1.5–2.0 K in built-up areas.

The thermal radiation from adjacent pixels significantly impacts ULST retrieval. This effect, characterized by inter-pixel interactions such as the mixed pixel problem and edge effect interference, introduces retrieval errors. Chen [11] confirmed that adjacent pixel thermal radiation substantially influences ULST retrieval from high-spatial-resolution thermal infrared (TIR) imagery and proposed a view-factor-based parameterization method. Ru [15] and Zhong [5] have also conducted parameterization studies on the adjacency effect using view factors. Zhong [5] investigated the adjacency effect using high-resolution drone data, revealing its impact on retrieved LST is 0.0–3.0 K. These findings underscore that the adjacency effect, arising from complex urban geometry, cannot be neglected. Despite current research methodologies for the adjacency effect being based on view factors and the average radiance of adjacent pixels, a systematic investigation into how urban geometry and materials influence this effect remains lacking.

Beyond the commonly discussed impacts of urban geometry and materials, the advancement of thermal infrared (TIR) remote sensing technology and the proliferation of high-resolution sensors (e.g., GF-5, SDGSAT-1) have increasingly highlighted the role of the adjacency effect in ULST retrieval. For instance, while GF-5 satellite TIR data (40 m resolution) captures finer details of the urban thermal field, radiation interference from adjacent buildings can significantly increase retrieval errors [11]. This demonstrates that estimating the adjacency effect necessitates consideration of spatial resolution [11]. Lower spatial resolution averages the thermal contrast between adjacent pixels, making the adjacency

effect more pronounced in high-resolution imagery. The current availability of data across various spatial resolutions raises a critical question: which spatial resolution is optimal for ULST retrieval? Zhen [16] investigated the optimal spatial resolution for ULST retrieval using the TES algorithm. Numerical experiments utilizing the DART model suggested that 30 m represents a key threshold for the existence of pure pixels in cities. Nevertheless, the optimal spatial resolution at which the adjacency effect can be neglected remains unclear. Therefore, this study systematically analyzed the influence of the adjacency effect under varying spatial resolutions, material properties, and thermal conditions.

This research employs numerical experiments based on the Discrete Anisotropic Radiative Transfer (DART) model to construct simulated urban scenes with diverse geometric and material characteristics, enabling systematic simulation and analysis of the adjacency effect. The DART model stands as one of the most comprehensive physically based 3D models for Earth–atmosphere radiative transfer, covering the spectral domain from ultraviolet to thermal infrared wavelengths [17]. It simulates the optical 3D radiation budget (RB) and can compute optical signals captured by proximal, aerial, and satellite imaging spectrometers and laser scanners, which is applicable to any urban or natural landscape and any experimental or instrumental configuration [18]. The DART model has been validated through a series of RAMI (RAdiation transfer Model Intercomparison) experiments [19], with its 3D radiative transfer capabilities verified in both the visible and thermal infrared domains. Leveraging the DART model, this study systematically simulated and analyzed the adjacency effect: scenarios were constructed combining different spatial resolutions (1–120 m), building geometric parameters (building height—BH, roof area index—λ_p, Surrounding Obstruction View Factor—$SVF_{Obs.}$), and material properties (reflectance R = 0.05, 0.10, 0.15) to quantify their impact on adjacency effects. The research aims to (1) elucidate the mechanisms by which geometric parameters (BH, λ_p, $SVF_{Obs.}$) and material properties ($\varepsilon = 1 - R$) govern the intensity of the adjacency effect; (2) determine the critical range of spatial resolution where the adjacency effect becomes negligible; and (3) evaluate the influence of surface component temperature differences.

This study employs the DART model to simulate the brightness temperature differences of target pixels under isolated and adjacent conditions, systematically analyzing the influence of spatial resolution, urban geometric structures, and other factors on the adjacency effects in urban land surface temperature (ULST) retrieval. The anticipated contributions include the following: (1) determining the critical spatial resolution range where adjacency effects become negligible, thereby providing a scientific basis for spatial resolution selection in current ULST retrieval processes; (2) clarifying the relative importance and individual effects of different factors on adjacent pixel interference, addressing existing gaps in factor analysis within current research; and (3) validating the conclusion that temperature differences among urban components exert minimal influence on adjacency effects, which offers theoretical support for simplifying ULST retrieval models. The findings are expected to provide a key foundation for developing more accurate ULST retrieval algorithms and optimizing remote sensing data selection (spatial resolution).

Section 2 describes the models used, the setup of the simulated scenes, and the employed formulas. Section 3 presents a summary and visualization of the experimental results, assessing the influence of different factors on the adjacency effect. Discussion of the results is provided in Section 4, and conclusions are drawn in Section 5.

2. Materials and Methods

2.1. Quantification of the Adjacent Pixel Effects

The study assumes that when only the target pixel exists in the environment (i.e., in an independent state), the observed thermal radiation L_{emit} originates solely from the target

pixel (Figure 1a). Under normal observation conditions (i.e., in a real-world scenario), the observed thermal radiation L_{canopy} originates from both the target pixel and its surrounding environment (Figure 1b).

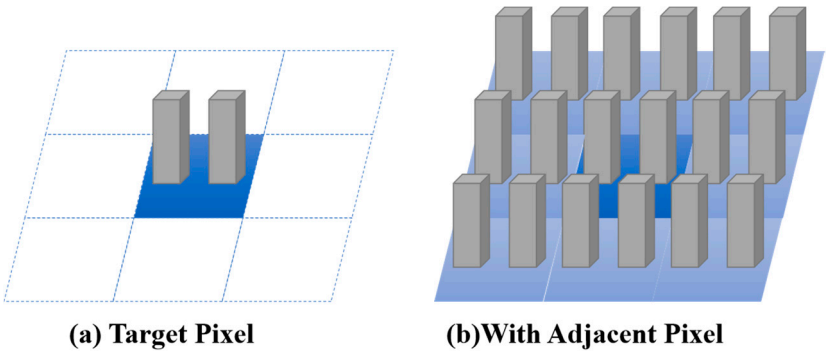

Figure 1. Comparison diagram of scene illustrations with and without the influence of adjacent pixels. (**a**) Isolated pixel: only the target pixel is present, and the observed radiance L_{emit} originates solely from the target pixel. In (**a**), the central dark-blue pixel denotes the target pixel, while the surrounding white pixels—lacking any geometric structure—indicate an empty neighborhood. (**b**) Real-world scene: the observed radiance L_{canopy} is the combined contribution from both the target pixel and its surrounding environment. In (**b**), the central dark-blue pixel remains the target pixel; the surrounding light-blue pixels, which bear geometric structures, signify the presence of neighboring objects.

In this study, the DART model was used to simulate the same target pixel under two states (shown in Figure 1) to obtain L_{emit}, L_{canopy}, and their corresponding simulated brightness temperatures. The adjacent pixel effect was quantified as the difference in simulated radiance and simulated brightness temperature between the two different states, which was used for subsequent analysis of influencing factors.

2.2. Parameterization of Building Structures

To quantitatively study how 3D structures influence the adjacent pixel effect, two parameters were used to describe the geometric structure of buildings: building height (BH, m) and roof area index (λ_p). Table 1 shows the symbols and abbreviations used in this paper.

$$\lambda_p = \frac{\sum_{i=1}^{n} S_i}{S} \quad (1)$$

where $\sum_{i=1}^{n} S_i$ represents the total area of all roofs, and S is the area of the horizontal section of the scene.

Table 1. Symbols and abbreviations.

Abbreviations, Symbols	Units	Description
BH	m	Building height
λ_p		Roof area index
Tb	K	Brightness temperature
L	$W \cdot m^{-2} \cdot sr^{-1} \cdot \mu m^{-1}$	Radiance
L_{emit}	$W \cdot m^{-2} \cdot sr^{-1} \cdot \mu m^{-1}$	Thermal emissions of urban target pixels
L_{canopy}	$W \cdot m^{-2} \cdot sr^{-1} \cdot \mu m^{-1}$	The radiance of urban canopy
SVF		Sky view factor
SVF_{in}		Openness within the target pixel
$SVF_{Obs.}$		Degree of obstruction of the target pixel by external adjacent pixels
R		Reflectance
T	K	Temperature
R_{same}		Material reflectance under identical material conditions
T_{same}	K	Material surface temperature under Isothermal condition
T_{roof}	K	Roof surface temperature
T_{wall}	K	Wall surface temperature
T_{ground}	K	Ground surface temperature
ε		Emissivity of the target pixel
$B(T_S)$		Planck's law, T_S is the surface temperature

The sky view factor (SVF), a commonly used urban morphological parameter that describes 3D structures, is defined as the ratio of radiation emitted (or received) by a scene to radiant energy received (or emitted) at the top of the hemispherical space above the scene [20]. The value of SVF ranges from 0 to 1. A value of 0 indicates that the central position is completely blocked (similar to a point inside a closed box, where no radiation can be emitted into the hemispherical space and there is no visible sky), while '1' indicates that the position is fully exposed to the sky (all the radiation can be emitted into the entire visible hemispherical space without any obstruction) [11]. Therefore, SVF can be extended to describe the degree of openness from the ground to the sky [21], which serves as a good supplement for using 3D morphological parameters in urban structure research.

To better study the radiant influence of adjacent pixels on urban target pixels, SVF_{in} and $SVF_{Obs.}$ (the degree of occlusion of adjacent structures on the target pixel) were used to represent the target pixel affected by the internal geometric structure of the pixel and adjacent pixels, respectively. SVF_{in} was used to characterize the openness within the pixel. That is, when calculating SVF_{in} in the independent state of the pixel, only the shielding effects by the components within the pixel were considered. In contrast, $SVF_{Obs.}$ was used to represent the degree of obstruction to the sky view of the target pixel by adjacent pixels. This obstruction mainly originates from each adjacent sub-pixel outside the target pixel [22] (Figure 2).

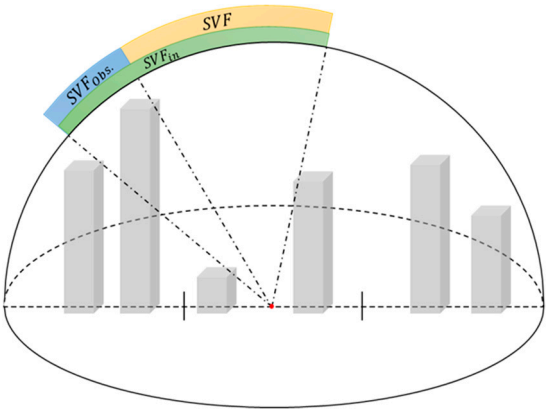

Figure 2. Diagram of the decomposition of the sky view factor (SVF) for radiation transfer research in urban environments. SVF_{in} is utilized to depict the openness inside the target pixel. $SVF_{Obs.}$ is employed to denote the extent to which neighboring pixels block the sky view of the target pixel.

In this study, SVF_{in} and $SVF_{Obs.}$ of the target pixel were used to quantify the impact of the geometric structure on the radiance/brightness temperature difference of the target pixel caused by the thermal emissions from the surrounding environment. The SVF calculation tools [23,24] were applied to calculate the SVF and SVFin required for this study, which were computed from the Digital Surface Model (DSM) of the simulated urban scene; $SVF_{Obs.}$ was calculated through Equation (2).

$$SVF = SVF_{in} - SVF_{Obs.} \quad (2)$$

2.3. Simulation of Radiation Transfer in Urban Scenes

2.3.1. The Simulation Tool: DART

Developed since 1992, the DART model (https://dart.omp.eu/#/, accessed on 20 August 2025) is one of the most comprehensive 3D radiative transfer models available. It simulates radiative transfer between the Earth's surface and the atmosphere, primarily covering radiative processes across the entire optical spectrum from ultraviolet (UV) to thermal infrared (TIR) [25].

In this study, simulations are configured with distinct properties assigned to different components. The graphical user interface (GUI) is used to define input parameters (e.g., atmospheric properties, scene attributes, solar position, sensor viewing geometry) and specify outputs (e.g., imagery, radiative budgets). Subsequently, simulated brightness temperature differences can be calculated based on the output results.

2.3.2. Simulation of Scene Structures

To study the influence of 3D structures on the adjacent pixel effects, the study adjusted the urban geometric parameters that incorporate radiation and thermal parameters. Input parameters for the DART model were set as follows:

1. Scene size and regularization of buildings: Each scene was set to a size of 30 m × 30 m, constructing a regular and symmetric scene composed of 4 identical flat-roofed rectangular buildings. Different roof area indices (λ_p) were achieved by altering the length and width of the buildings. The building heights were incrementally increased from 10 m to 40 m (Figure 3).
2. Simulation of the target pixel in two states: The simulation of the adjacent pixel effects was accomplished by modifying the parameter of "repetition times of user-defined scenes" in the DART model. Setting this parameter to "0" and "1" simulated independent, non-repeating urban cubes and infinite cyclic urban landscapes, respectively.
3. The urban scene consisted of three components: roofs, walls, and the ground, all of which were Lambertian surfaces (Figure 4). Under isothermal conditions, each component had constant temperature (T/Tsame) and material emissivity (R/Rsame). Otherwise, different components had different emissivities (R roof, R wall, R ground) and temperatures (T roof, T wall, T ground).
4. In this study, solar and atmospheric thermal emissions were not considered; thermal emissions originated solely from the city itself, namely, the simulation was conducted under the "Mode T" condition without the atmosphere. The experiment simulated the radiance/brightness temperature images at a wavelength of 10 μm.

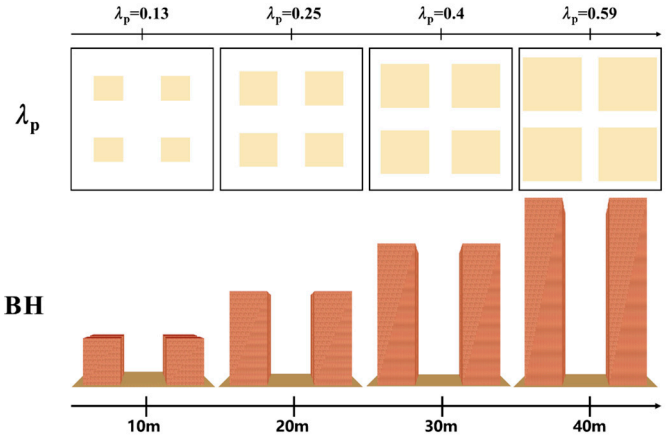

Figure 3. Three-dimensional urban scenes created in DART are used to study the impact of urban structure on the adjacent pixel effect. BH represents the building height, and λ_p represents the ratio of the total roof area of the building to the total plane area of the scene. They are grouped in pairs and numbered from G1 to G16. For G1–G4, λ_p = 0.13, and BH values increase from 10 m, 20 m, 30 m, to 40 m, successively; for G5–G8, λ_p = 0.25, and BH values increase from 10 m, 20 m, 30 m, to 40 m, successively; for G9–G12, λ_p = 0.40, and BH values increase from 10 m, 20 m, 30 m, to 40 m, successively; for G13–G16, λ_p = 0.59, and BH values increase from 10 m, 20 m, 30 m, to 40 m, successively.

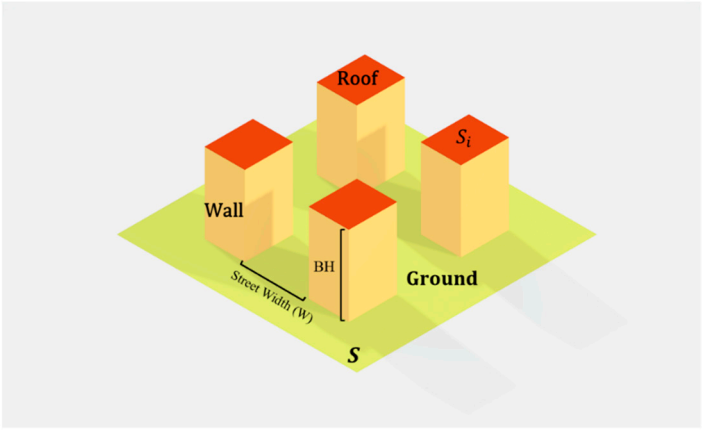

Figure 4. Three-dimensional urban model is presented, where the road width is denoted as W, the wall height as H, and the area of the horizontal section of the scene as S. Under isothermal conditions, the surface reflectance is R/Rsame, and the surface temperature is T/Tsame. Under non-isothermal conditions, each wall, road, and roof has its own surface reflectance and surface temperature.

Ultimately, 16 scenes of 3D geometric configurations were constructed. The geometric parameters were set as follows: BH (m) took values of 10, 20, 30, and 40; and λ_p took values of 0.13, 0.25, 0.4, and 0.59, aiming to explore the relationship between geometric structure parameters and the adjacent pixel effect.

Figure 5 presents the workflow for simulating the adjacency effect based on the DART model. Sixteen standard 3D urban scenes (30 m × 30 m) were first constructed, with building heights ranging from 10 to 40 m, roof-area indices from 0.13 to 0.59, and surface material reflectances of 0.05, 0.10, and 0.15. Simulations were then performed in no-atmosphere "thermal-T" mode at 10 µm. Spatial resolution was controlled (1–30 m) by adjusting (i) the scene replication count (0 = isolated pixel, 1 = pixel including neighbors) and (ii) the sensor sampling interval. Finally, DART computed the brightness temperature from the outgoing radiance using Planck's law, and the adjacency effect was quantified as ΔTb, the difference in simulated brightness temperature between the pixel influenced by its neighbors and the isolated pixel.

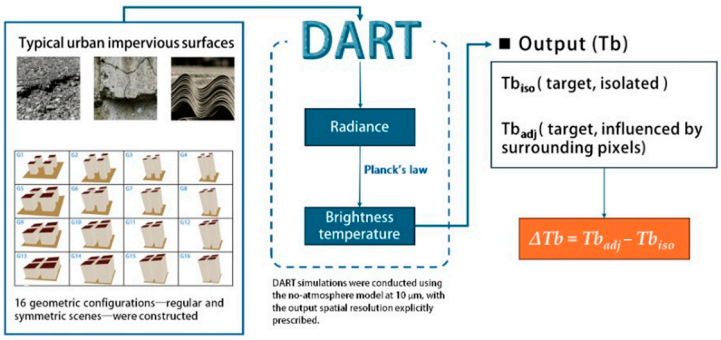

Figure 5. Flowchart of adjacent pixel effect simulation using DART model.

2.4. Emissivity of Typical Urban Materials

Significant variations can be caused by different categories among anthropogenic materials [26]. We searched and compiled the emissivity of ten material categories (e.g., granite, cement, asphalt) from the ASTER Spectral Library (https://speclib.jpl.nasa.gov, accessed on 15 August 2025) and the LUMA Spectral Library [26,27]. The emissivity of the materials at 10 μm was statistically analyzed. Figure 6 shows that the emissivity of over 50% of common impervious surface materials (anthropogenic materials) is distributed around 0.9, and most of them are in the range of 0.95 to 1. Most of the materials with a reflectance close to 1 are metallic aluminum and metallic silver, which are used for making roofs. Through statistics, to make the study close to reality, the reflectance of the experimental materials was set to 0.05, 0.1, and 0.15 to study the impact of different materials on the adjacent effect. Since the sum of absorbance and reflectance of the ground objects is equal to '1' at 10 μm, the emissivity is calculated as '1-reflectance' [28].

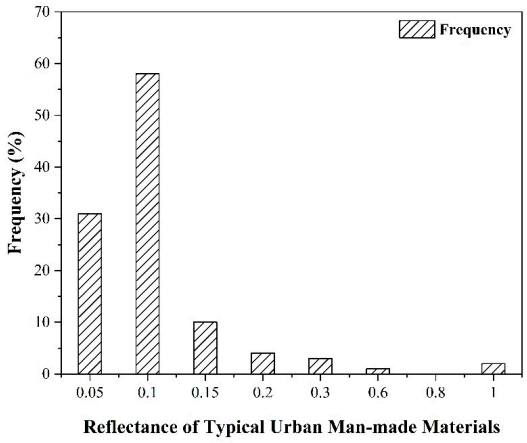

Figure 6. Frequency distribution of the reflectance of typical urban man-made materials.

3. Results

3.1. The Influence of Spatial Resolution on the Adjacent Pixel Effects

The statistical distribution results of the simulated brightness temperature differences (ΔTb) from adjacent pixel effects at different spatial resolutions (Figure 7) reveal two key trends. Firstly, the mean ΔTb decreases as resolution coarsens, with the highest (>5 K) at 1 m resolution and the lowest (<2 K) at 30 m resolution. Secondly, the interquartile range (IQR) values of ΔTb progressively decrease from high to low spatial resolutions: 2.7577, 2.4130, 1.7060, 1.2639, 1.2460, and 1.0298. This indicates a narrowing range of ΔTb values and a reduction in outliers as resolution decreases. Consequently, these findings demonstrate that the adjacent pixel effects are more pronounced at higher spatial resolutions, reflecting their capability to capture finer-scale brightness temperature variations (e.g., building geometry

and surface material properties). In contrast, at lower spatial resolutions, the 'smoothed out' effect of within-pixel heterogeneity leads to an averaging of brightness temperature differences, thereby weakening the discernible features of the adjacent pixel effects.

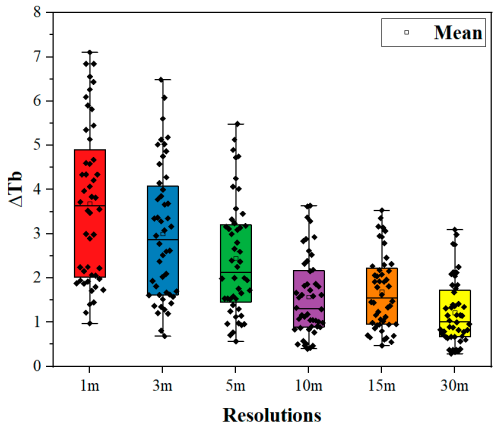

Figure 7. The simulated brightness temperature difference (ΔTb) induced by adjacent pixel effects across different spatial resolutions, encompassing scenarios with varying material properties and 3D structures. The black squares represent the simulated ΔTb of target pixels with varying geometric structures and materials at the given spatial resolution.

3.2. The Impact of 3D Structure on the Adjacent Pixel Effects

Figure 8 illustrates the relationship between building geometric metrics and adjacent pixel effects, and Figure 9 presents that for SVF. Figure 8 reveals that an increase in building height (BH) enhances the influence of adjacent pixels on the target pixel's brightness temperature (with higher spatial resolutions exhibiting greater sensitivity). Conversely, an increase in roof area index (λ_p) diminishes this influence, with adjacent pixel effects being more pronounced at higher resolutions.

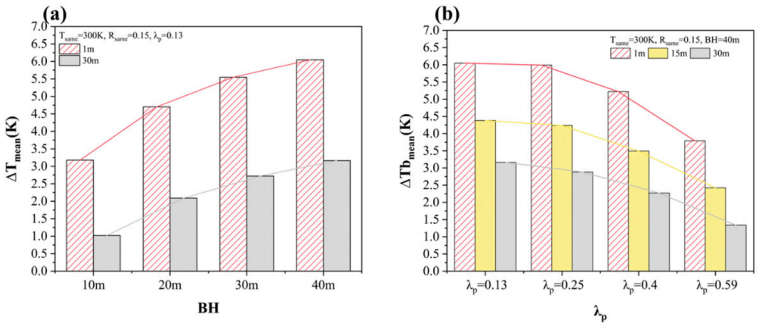

Figure 8. The average impact of different structural parameters on the adjacent pixel effect at high and low spatial resolutions, ΔTb_{mean}; (**a**) the average impact of building height on the adjacent pixel effect; (**b**) the average impact of λ_p on the adjacent pixel effect.

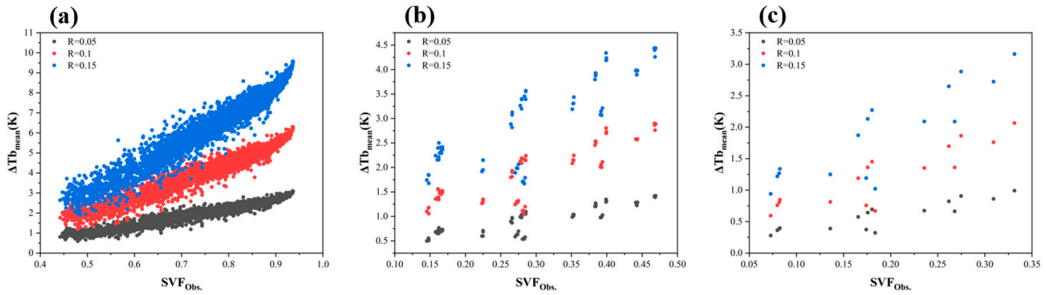

Figure 9. The relationship between $SVF_{Obs.}$ and the average change in brightness temperature (ΔTb_{mean}) of the target pixel caused by the adjacent pixel effect at different spatial resolutions. (**a**) The results at 1 m spatial resolutions. (**b**) The results at 15 m spatial resolutions. (**c**) The results at 30 m spatial resolutions.

Figure 9 shows the relationship between $SVF_{Obs.}$ and ΔTb for different materials under isothermal conditions (T = 300 K) at 1 m, 15 m, and 30 m resolutions. Higher spatial resolutions correspond to a larger range of $SVF_{Obs.}$ values and greater obstruction of the target pixel by adjacent structures. Within the same resolution, material properties exert a significant influence; specifically, larger $SVF_{Obs.}$ values (indicating greater obstruction) correlate with stronger adjacent pixel effects (higher ΔTb). Under the isothermal condition (T = 300 K), the attainable range of $SVF_{Obs.}$ for the target pixel varies with spatial resolution and expands as resolution increases: 0.43–0.94 at 1 m, 0.145–0.47 at 15 m, and 0.08–0.33 at 30 m. This confirms that higher resolutions experience more severe obstruction from adjacent structures. At 15 m resolution, for instance, as $SVF_{Obs.}$ increases from 0.15 to 0.5, ΔTb rises from 1.67 K to 4.44 K for higher-reflectance materials (Figure 9a). Similar $SVF_{Obs.}$-ΔTb relationships are observed at other resolutions. In summary, $SVF_{Obs.}$ of the target pixel is intrinsically linked to spatial resolution. Furthermore, at a given resolution, material properties significantly modulate the adjacent pixel effects, with larger $SVF_{Obs.}$ values (greater obstruction) leading to a stronger influence of adjacent pixels on the target pixel.

3.3. Influence of Material Emissive Properties and Thermal Heterogeneity

Figure 10 demonstrates the influence of material reflectance on the adjacent pixel effect. The results show that increased material reflectance (i.e., reduced emissivity) intensifies the adjacent pixel effect on the target pixel. For configuration G1 (λ_p = 0.13, BH = 10 m), the brightness temperature differences (ΔTb) are 0.33 K, 0.67 K, and 1.04 K for reflectance values of (R) = 0.05, 0.1, and 0.15, respectively. Furthermore, (a) at fixed λ_p = 0.13, ΔTb variations (>2 K) induced by differing R exceed those caused by building height variations (G1–G4: BH = 10/20/30/40 m, ΔTb < 1 K). (b) At fixed BH = 20 m, ΔTb variations (>1.5 K) from differing R surpass those from roof area index variations (G2/G6/G10/G14: λ_p = 0.13/0.25/0.4/0.59, ΔTb < 0.5 K). Collectively, reduced material emissivity significantly enhances adjacent pixel effects, with material emissivity exerting a stronger influence than both building height (BH) and roof area index (λ_p).

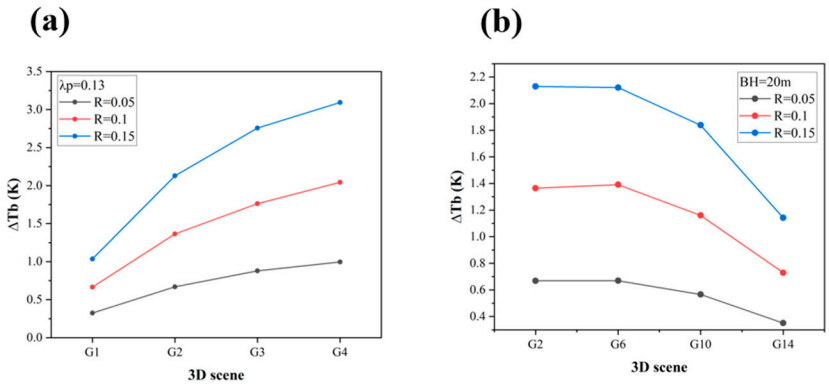

Figure 10. The influence of material reflectance on the adjacent pixel effects. (**a**) Impact of material reflectance on brightness temperature difference (ΔTb) for configurations G1/G2/G3/G4 (λ_p = 0.13, BH = 10 m/20 m/30 m/40 m); (**b**) impact of material reflectance on ΔTb for configurations G2/G6/G10/G14 (BH = 20 m, λ_p = 0.13/0.25/0.4/0.59).

Subsequently, Figure 11 examines the surface temperature impacts under isothermal conditions. When uniformly increasing surface temperature from 285 K to 305 K, the maximum brightness temperature increase is merely 0.75 K. Thus, temperature effects on adjacency are negligible under isothermal assumptions.

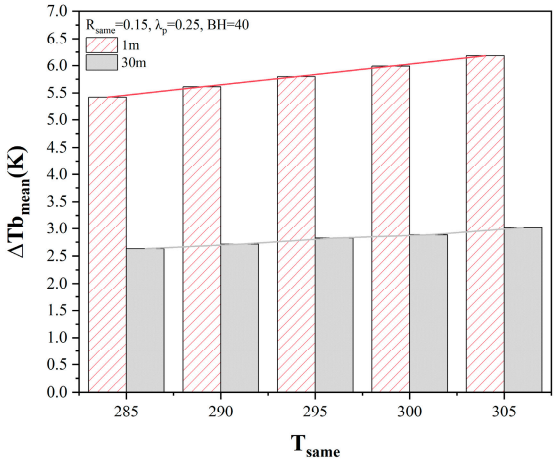

Figure 11. The impact of temperature on the adjacent pixel effect, ΔTb_{mean}, in an isothermal scene.

4. Discussion

In Section 3, we present the relationship between adjacency effects and various factors in radiative simulations of the urban scenario described in Section 2.3. However, these simulations employ symmetrically and regularly distributed buildings, which can only yield simplified relationships and fail to fully capture the complexity of real-world urban environments. Therefore, in Section 4, we will adjust multiple factors—including incorporating higher spatial resolution, introducing real DSM data, and setting temperature differences among urban component surfaces—to analyze whether the aforementioned findings remain applicable in the investigation of complex urban scenarios.

4.1. Impacts of Multiple Factors on Adjacent Pixel Effects

Previous research on retrieving ULST from thermal infrared (TIR) imagery has highlighted the non-negligible influence of adjacent pixels in high-spatial-resolution remote sensing data [29]. This study aims to investigate the impact of various factors on adjacent pixel effects. By employing the DART model, we simulated the brightness temperature difference (ΔTb) of a target pixel induced by adjacent pixels under varying spatial res-

olutions, urban geometric structures, and material surface properties. The simulations, interpreted from a radiative transfer perspective, elucidate how energy from adjacent geometric structures influences the target pixel under different factors. Compared to prior studies, this work further reveals the influence mechanisms of spatial resolution, 3D structural parameters (building height, roof area index, and obstruction level), and material properties (emissivity and surface temperature).

4.1.1. Discussions on Other Spatial Resolutions

In Section 3.1, we simulated the target pixel's ΔTb across 1–30 m spatial resolutions. It was found that while the target pixel's sensitivity to energy from adjacent pixels is less pronounced at 30 m resolution compared to higher resolutions, ΔTb serves as a quantitative metric for adjacent pixel effects. Figure 12 illustrates the frequency distribution of ΔTb across different spatial resolutions, which directly reflects variations in adjacency effect intensity. The 30 m resolution demarcates higher and lower resolutions based on ΔTb magnitude: In high ΔTb intervals (>1.5 K), frequencies exceed 20% for resolutions finer than 30 m but fall below 10% for coarser resolutions. Conversely, in low ΔTb intervals, approximately 50% of cases fall within 0–1 K, decreasing to 23% in the 1–1.5 K range, showing significant cross-interval fluctuation. Compared to high resolutions (e.g., 1 m, 3 m), the 30 m resolution exhibits a steeper gradient in ΔTb frequency distribution across intervals, validating the findings of Zhen [16] showing that 30 m represents the spatial resolution where adjacent pixel effects exhibit the most significant variation within geometrically complex mixed pixels. However, as indicated by the fluorescent yellow polyline in Figure 12, ΔTb exceeding 1 K accounted for 68.75% of all simulated cases at 30 m resolution. Notably, a substantial portion reached 2 K, with specific geometric configurations (minimum building density and maximum building height) yielding ΔTb > 3 K. This indicates that 30 m resolution is not yet the critical threshold where adjacent pixel effects can be neglected in ULST retrieval. This result aligns with Chen [11], who concluded that adjacent pixel effects must be considered for ULST retrieval from high-resolution TIR data like GF-5's 40 m imagery.

To more precisely identify the critical spatial resolution range where adjacent pixel effects significantly impact the target pixel, we extended the simulations to include 60 m, 90 m, and 120 m resolutions. Under isothermal conditions with reflectances of R = 0.05, 0.1, and 0.15, frequency statistics of the target pixel's ΔTb at 60 m, 90 m, and 120 m are presented in Figure 12. It can be observed that at these lower spatial resolutions, over 70% of target pixels exhibited ΔTb < 1 K. At 90 m resolution (Figure 12), adjacent pixel effects induced ΔTb > 1 K only under exceptionally prominent urban geometric structures; in all other cases, ΔTb remained below 1 K. Consequently, we therefore regard the 60–90 m range as the threshold at which the adjacency-induced error is attenuated to a level that is commensurate with the intrinsic uncertainty of current mainstream ULST algorithms (1–2 K for split-window methods) and thus acceptable for many urban heat island analyses.

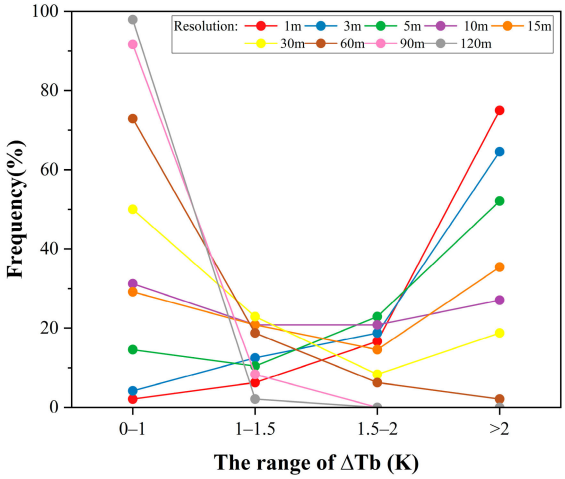

Figure 12. The frequency distribution of ΔTb across different spatial resolutions.

In order to substantiate the proposed critical range, an additional experiment was conducted by randomly selecting a practical study area (Hong Kong, China), with target pixels at spatial resolutions of 40 m and 80 m. The experiment is explicitly designed to verify the aforementioned critical range of spatial resolution; accordingly, material reflectance is fixed at 0.1 to eliminate its confounding influence. This material property selection first refers to the common reflectance values of urban materials (0.05/0.1/0.15) statistically summarized in Section 2.4. Secondly, concrete and cement account for a significantly high proportion (close to or exceeding most cases) in local building exterior walls and structures, and their corresponding parameters (ε = 0.9, R = 0.1) can represent the mainstream properties of urban surfaces. The building surface inputs for the experiment were derived from Hong Kong DSM data sourced from a spatial data sharing platform (https://portal.csdi.gov.hk/csdi-webpage, accessed on 29 August 2025). The adjacency effect was characterized by the simulated ΔTb under isothermal and homogeneous conditions (T = 300 K, R = 0.1). Figure 13 shows that at the 40 m spatial resolution, the Tb of the target pixel in an isolated state was 296.72 K, while under the influence of the surrounding environment, it was 297.49 K, resulting in a ΔTb of 0.77 K due to geometric and adjacency effects. At the 80 m spatial resolution, the Tb of the target pixel in isolation was 297.07 K, increasing to 297.37 K when influenced by the surrounding environment, yielding a ΔTb of 0.30 K. These results demonstrate consistency with the findings in Section 3.1: a higher spatial resolution (40 m) captures a more pronounced ΔTb induced by geometric and adjacency effects. At finer resolutions, pixels represent smaller ground areas, enabling a more detailed representation of ground heterogeneity and making the influence of heat exchange between environments more evident. Conversely, at coarser resolutions (80 m), the larger pixel coverage dilutes the manifestation of these effects. That is, pixels are more significantly impacted by their surroundings at high spatial resolutions, while at lower resolutions, they are less disturbed and approach their isolated Tb state. Under actual complex geometric structures, the 80 m spatial resolution remains consistent with the discussed critical range of 60–90 m. Although the 80 m resolution in this experiment may not represent an exact threshold for neglecting adjacency effects, it still provides a valuable reference for subsequent research.

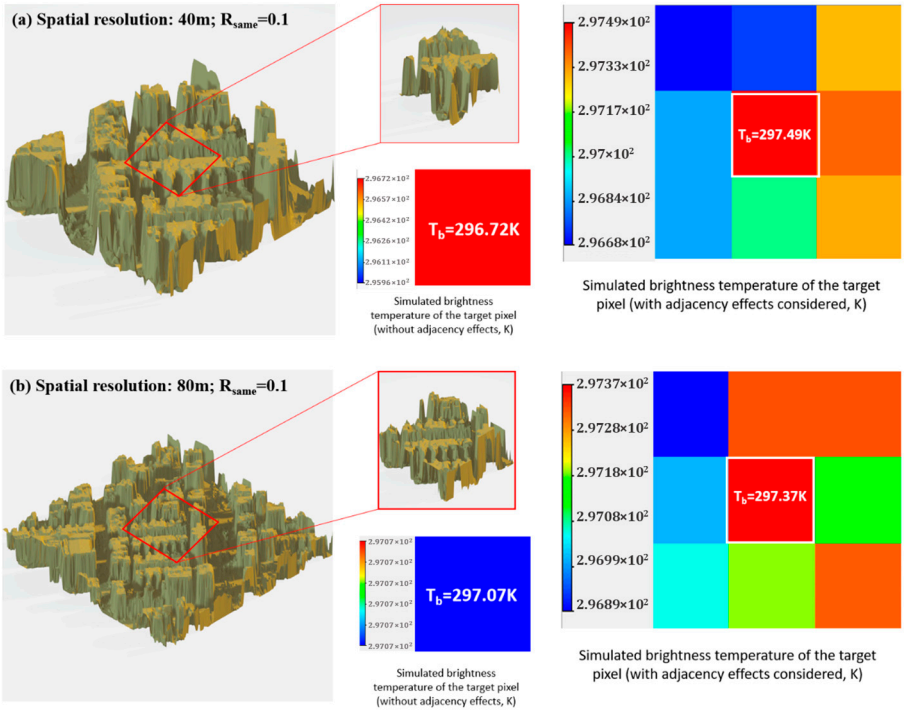

Figure 13. Actual DSM data of Hong Kong region (randomly selected study area): simulated brightness temperature maps of the target pixel and its surrounding environment at 40 m and 80 m spatial resolutions.

4.1.2. Analysis of Geometric Structure on Adjacency Effects

Regarding urban geometric structure, the results in Section 3.2 are based on simulations assuming uniformly regular distributed buildings. This controlled setup facilitated a clearer analysis of the correlation between the target pixel's structural parameters and adjacent pixel effects. The findings in Section 3.2 indicate that adjacent pixel effects become more pronounced with increasing building height and decreasing building density (λ_p). These trends are related to the void space within the target pixel (the 3D space formed between building facets and the urban ground plane). When adjacent geometric structures reflect energy towards the target pixel, not all reflected energy is received by the target pixel; only a portion enters and persistently influences it. Energy entering the target pixel's internal structure undergoes multiple reflections between walls and the ground due to the void space. During these reflections, energy is partially absorbed by the internal materials due to their absorption properties. This ultimately manifests as an increase in the total absorbed radiance observed for the target pixel. Lower building density widens the "pathway" for reflected energy from adjacent structures to enter the target pixel. Increased building height provides more opportunities for the energy entering the target pixel to be reflected, accompanied by partial absorption, thereby increasing the overall radiance.

Furthermore, while the UCM-RT model proposed by Chen [11] introduced SVF_{in} and SVF_{adj} as fundamental descriptors for energy exchange between the target pixel and its surroundings—variables also commonly used in most adjacent pixel effects studies—this study diverges by employing the sky view factor obstructed by adjacent structures ($SVF_{Obs.}$). The sky view factor of a target pixel depends on both its internal structure and external obstruction by surrounding structures. Therefore, we directly utilize this external obstruction metric to describe and quantify the portion influenced by adjacent pixels. Greater obstruction of the target pixel by adjacent structures (lower $SVF_{Obs.}$) corresponds to more energy reflected back to the target pixel, leading to more significant adjacent pixel effects. This aligns with the findings of Chen [11] regarding the significant impact of $SVF_{Obs.}$ on ground

temperature and Top-Of-Atmosphere (TOA) brightness temperature, where a decrease in SVF_{adj} (implying reduced sky view for adjacent pixels and thus more reflection towards the target) increases the contribution of scattered radiance from adjacent pixels.

However, the findings presented in Section 3 of this study were derived from simulations under idealized, symmetric urban building structures. To investigate the relationship between geometric structure and adjacency effects under more realistic conditions, we further examined the relationship between the observed sky view factor ($SVF_{Obs.}$) and the resulting brightness temperature change (ΔTb) of the target pixel due to adjacency effects, under isothermal and homogeneous conditions at a spatial resolution of 40 m. The focus of this experiment is on the impact of geometric structures on the adjacency effect of adjacent pixels. To avoid interference, all experiments on real urban surfaces will unify the material properties to ensure that the geometric structure is the only variable; therefore, the surface reflectance of the material is still fixed at 0.1, and the basis for selecting this parameter value is consistent with that described in Section 4.1.1 (line 401). The building surface inputs for this experiment utilized DSM data of Hong Kong, sourced from a spatial data sharing platform (https://portal.csdi.gov.hk/csdi-webpage, accessed on 29 August 2025). Five randomly selected areas (40 m × 40 m), designated HK_1 to HK_5, served as the study objects. Consistent with the findings in Section 3.2 across various spatial resolutions, an increase in $SVF_{Obs.}$ was found to correspond to an increase in ΔTb. This indicates that greater obstruction of the target pixel by surrounding structures leads to a more pronounced influence from adjacency effects. Figure 14 confirms that this influence pattern also holds at the 40 m resolution. Overall, ΔTb exhibits an increasing trend with higher $SVF_{Obs.}$. Nevertheless, within these five randomly selected study areas, the variation in brightness temperature difference (ΔTb) does not demonstrate a strictly monotonic relationship with $SVF_{Obs.}$. This deviation contrasts with the results in Sections 3.1 and 3.2, which were obtained under regular urban scenarios exhibiting relatively distinct linear relationships. The irregular urban surfaces examined here involve more complex thermal interactions between components. In real urban environments, the relationship between $SVF_{Obs.}$ and ΔTb exhibits localized deviations from monotonicity. Although the overall trend remains largely consistent, irregular building geometries—such as asymmetrical heights, misaligned orientations, and abrupt variations in obstruction angles—disrupt the idealized multiple-scattering pathways. These structural heterogeneities alter radiation propagation within the urban canopy, leading to complex trajectories of scattered energy and localized fluctuations in ΔTb, even under uniform surface temperatures and material properties. Notably, such non-monotonic behavior often occurs among pixels with similar $SVF_{Obs.}$ values, underscoring the critical importance of 3D morphological variations beyond $SVF_{Obs.}$ itself. Therefore, accurate simulation in real urban settings requires geometric descriptors capable of capturing both intricate spatial arrangements and mutual obstructions among buildings.

4.1.3. Analysis of Non-Isothermal Surfaces on Adjacency Effects

Regarding material properties, Zhong [5], utilizing UAV data, indicated that adjacent pixel effects are influenced by the target pixel's emissivity and the surrounding environment, with pixels of lower emissivity being more significantly affected. Under isothermal conditions in Section 3.3 of this study, we simulated different material reflectances (R = 0.05, 0.1, 0.15). The results corroborated the above conclusion, demonstrating the universality of this pattern across different urban morphologies. Critically, the simulations revealed that material properties exert a stronger influence on adjacent pixel effects than urban structural parameters.

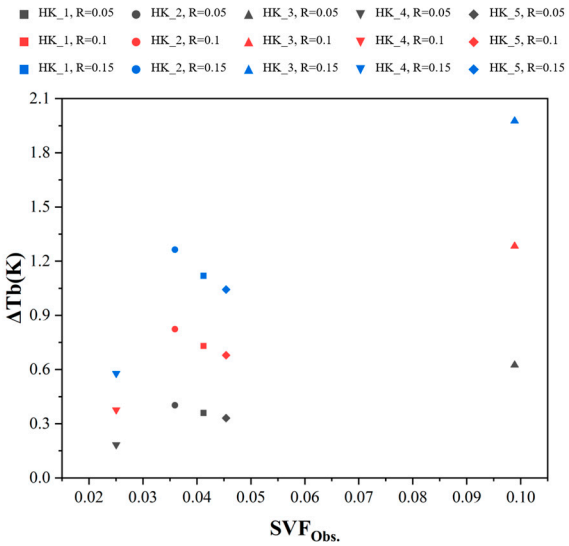

Figure 14. Actual DSM data of Hong Kong region (five randomly selected zones): relationship between observed sky view factor ($SVF_{Obs.}$) and simulated brightness temperature difference of the target pixel (at 40 m spatial resolution) induced by adjacency effects.

The preceding discussions were conducted under isothermal conditions. However, in reality, component temperatures exhibit significant non-isothermicity due to factors such as solar radiation incidence, orientation, and surface area. To investigate the applicability of the isothermal findings and quantify the impact of surface component non-isothermicity on adjacent pixel effects across spatial resolutions, we introduced temperature differences between components. Typically, roofs exhibit higher temperatures, walls are cooler, and ground surfaces fall in between. Consequently, temperatures were set to 315 K for roofs, 310 K for ground surfaces, and 300 K for walls as inputs for the DART simulations. The results demonstrated that differences in component temperatures have a negligible impact on adjacent pixel effects (<0.5 K ΔTb, mostly <0.1 K at lower resolutions), indicating that the conclusions derived from isothermal surfaces remain applicable. Figure 15 illustrates this for the same scene, comparing isothermal and non-isothermal surfaces. Although warmer ground surfaces radiate more energy compared to cooler walls, potentially increasing the radiation impacting adjacent pixels, the resulting difference in adjacent pixel effects due to the temperature contrast between 3D building facets and ground surfaces proved minimal and comparable to the isothermal case. Furthermore, the disparity in adjacent pixel effects between the two scenarios (isothermal vs. non-isothermal) is very small at low spatial resolutions (below 30 m). Therefore, within the identified critical spatial resolution threshold range (60–90 m), the isothermal assumption can reasonably be employed to simplify the quantification of adjacent pixel effects.

4.2. Significance of Simulation and Potential Improvements

High-spatial-resolution remote sensing imagery now offers finer details of the thermal environment. However, for large-scale thermal environment assessment, evaluating the adjacent pixel effects remains crucial. The preceding analysis—conducted on regularized scenes with uniform building height—shows that, within the 60–90 m resolution window, the adjacency-induced error drops below 1 K in the majority of cases, rendering the effect operationally manageable rather than negligible. We emphasize that these results are most valid for relatively homogeneous urban layouts and should be re-evaluated for highly heterogeneous environments before wider application. Furthermore, material emissivity was found to exert a more pronounced influence on the magnitude of adjacent pixel effects compared to geometric structure. Although the relationships between various factors and

adjacent pixel effects were established through simulation, several key aspects require further consideration and refinement to be overcome in the future.

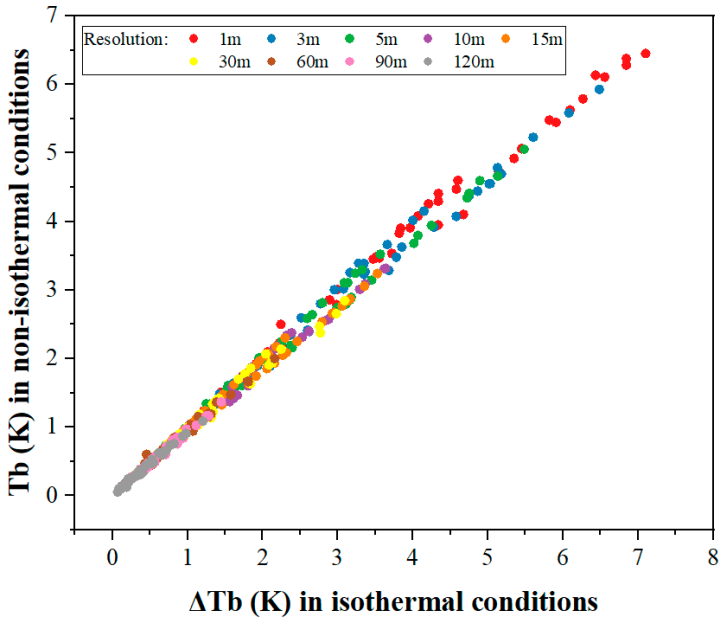

Figure 15. The comparison of adjacent pixel effects under both isothermal and non-isothermal conditions for the same scene.

First, in existing simulations, material spectra and building morphology are often simplified to a "single emissivity + regular array" configuration, which significantly deviates from the complex underlying surfaces of real urban areas. To quantitatively evaluate the uncertainty introduced by such simplifications, we further incorporated random materials (multiple samples labeled as artificial materials from the ASTER spectral library, which exhibit diverse optical properties in the 10 μm simulation band) and more realistic building data, conducting a preliminary simulation of the adjacency effect at a spatial resolution of 30 m. Even under the isothermal surface assumption, the results in Figure 16 show that the temperature differences for most target pixels reached 2–3 K, with a full range of 0–15 K, significantly higher than the idealized results (0–4 K) presented in the yellow box in Figure 7. The simulation in Figure 7 is based on the assumptions of "isothermal, homogeneous materials, and regular geometry," whereas the irregular substrates, varying building heights, and the resulting spatial heterogeneity in SVF in real urban areas markedly enhance the multiple scattering and reflection processes of thermal radiation [30]. Moreover, unifying material emissivity diminishes the radiative difference signals between adjacent pixels, leading to a systematic underestimation of the adjacency effect, which should otherwise be pronounced. Such temperature differences, co-modulated by "material-geometry" details, are typical features revealed in refined urban thermal environment studies. Therefore, future research should utilize high-resolution 3D building models or aerial LiDAR data to more accurately characterize urban structural details. Simultaneously, a more comprehensive urban feature spectral library should be introduced, coupled with laboratory-measured hyperspectral emissivity data, to assign more precise optical and thermal parameters to surfaces of different materials and aging stages, thereby enhancing the model's universality and retrieval accuracy for real urban underlying surfaces.

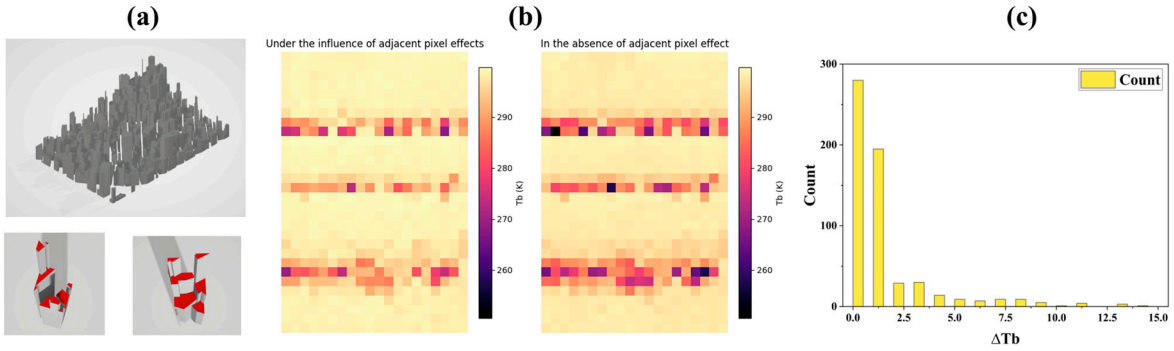

Figure 16. Under isothermal conditions, simulations performed for the scenario constructed from more randomized materials and more realistic building data, at a spatial resolution of 30 m for ΔTb. (**a**) An isometric left-side view of the real building data employed for the simulations, along with two 30 m × 30 m sub-domains extracted therefrom. (**b**) On the left, the simulated brightness temperature map influenced by the adjacency effect, and on the right, the mosaic obtained by simulating each sub-domain independently (i.e., free of adjacency effects). (**c**) The statistical histogram of the brightness temperature differences between the two aforementioned simulation states.

Second, the urban thermal environment is shaped by multiple underlying surfaces such as buildings, vegetation, and water bodies. This study intentionally focuses on the built-up structures in urban areas, where the 3D configuration of buildings, the materials they are made of, and the spatial resolution-induced spectral mixing of these structures in imagery are the core factors to be analyzed. For the purposes of this research, vegetation and water bodies are temporarily simplified as background elements, as they generally exhibit relatively flat morphology and lack the "cavity structures" (which are present in buildings) that generate multiple scattering. Nevertheless, transpiration from vegetation and the thermal inertia of water bodies continue to influence the temperature field through distinct thermal radiation and energy exchange processes. Therefore, incorporating a wider range of surface components would enable a more comprehensive characterization of how adjacent pixels influence the target pixel.

Finally, validation against field measurements such as ground-based thermal infrared observations or UAV remote sensing remains an indispensable yet missing step of the present study. However, the DART model employed in our simulations has already undergone a three-way validation against flux–brightness temperature–directionality, e.g., Widlowski [31] cross-compared DART with eleven 3D Monte Carlo models within the RAMI-III exercise over heterogeneous vegetation and urban structures and reported reflectance relative discrepancies $\leq$1%, and Sobrino [32] further validated DART-derived brightness temperatures over bare soil, grassland, and urban scenes using airborne AHS and satellite ASTER data together with ground stations, achieving root-mean-square errors <2 K. These results confirm the applicability of DART to real 3D urban structures, hence its usability in thermal infrared remote sensing. Nevertheless, direct comparison between simulations and real-world scenes still confronts several practical barriers. First, temporal mismatch and consistency issues—such as asynchronous satellite overpass and ground observation times, divergent atmospheric conditions, and inconsistent spectral/field-of-view characteristics of instruments—introduce systematic biases. Second, inherent confounding factors in imagery, e.g., uncertainties in surface emissivity retrieval and unresolved mixed pixels, further complicate the validation. Consequently, future multi-source data fusion strategies (e.g., coupling mobile ground campaigns with coordinated satellite acquisitions) are required to address these challenges. Moreover, rigorous validation itself remains a topic that warrants continuous investigation, demanding iterative refinement of ULST retrieval algorithms and a deeper interpretation of radiative transfer processes.

5. Conclusions

This study used the DART model to simulate the brightness temperature differences of target pixels under different spatial resolutions, 3D structures, and materials and characterize the adjacent pixel effect in urban areas. The main conclusions are as follows:

1. Critical spatial resolution of the adjacent pixel effect. With the increase in spatial resolution, target pixels become more sensitive to the energy reflected by adjacent pixels. The threshold for significant adjacent pixel effects is near 30 m spatial resolution. In the inversion process, there exists a critical spatial resolution range of 60–90 m where the adjacency-induced error is attenuated to a level ($\Delta Tb < 1$ K) that is commensurate with the intrinsic uncertainty of current mainstream ULST algorithms and thus acceptable for many urban heat island analyses, allowing the inversion process to be simplified by ignoring the adjacent pixel effect.
2. Structure and adjacent pixel effect. A decrease in building density and an increase in building height increase the opportunity for energy reflected by adjacent pixels to enter the target pixel and enhance the possibility of multiple scattering within the target pixel, respectively, thereby increasing the overall radiative energy of the target pixel. This leads to an increase in the adjacent pixel effect. Meanwhile, the greater the degree of occlusion of the target pixel by adjacent pixels, the more pronounced the adjacent pixel effect.
3. Material and adjacent pixel effect. In simulations of isothermal surfaces, the adjacent pixel effect is more significant for low-emissivity materials. Among the influencing factors of the adjacent pixel effect, the difference in material emissivity itself outweighs the scattering influence of the geometric structures of adjacent and target pixels.
4. The rule-based simulations offer direct guidance for operational use. First, at resolutions finer than 30 m, the adjacency effect is pronounced; explicit correction is strongly recommended to obtain physically meaningful ULST. Second, within the 60–90 m range, the effect is markedly attenuated, and investigators may omit adjacency correction if the study can tolerate an additional uncertainty of $\leq$1 K. We caution, however, that applications demanding the highest accuracy—such as fine-scale analyses of heat island mechanisms—should still evaluate and correct for adjacency even when the resolution is coarser than 90 m. These conclusions were derived from regularized scenes with uniform building height and are most applicable to relatively homogeneous urban layouts. Although we corroborated the 60–90 m threshold using real-world DSM data (Section 4.1.1), the results should be re-evaluated for highly heterogeneous environments.

By reasonably setting factor variations and simulating the adjacent pixel effect via the DART model, we quantified the adjacent pixel effect more clearly under different spatial resolutions, 3D structures, and materials, providing a scientific basis for simplifying the urban land surface temperature inversion process. Future research should further consider building material properties and the configuration of more urban components (such as vegetation or water). Additionally, simulations should account for more realistic and complex urban geometric conditions, requiring the fusion of multi-source data for improvement.

Author Contributions: Conceptualization, J.Y. and Y.X.; methodology, L.F., J.Y. and X.O.; software, L.F. and J.Y.; validation, L.F., J.Y. and L.Z.; writing—original draft preparation, L.F. and J.Y.; writing—review and editing, Q.S. and M.M.; supervision, J.Y.; project administration, Q.S.; funding acquisition, Q.S., J.Y., X.O. and Y.X. All authors have read and agreed to the published version of the manuscript.

Funding: This work was supported by grants from the National Natural Science Foundation of China (grant nos. 42222106, 42271345, 42171370, and 42271477).

Conflicts of Interest: The authors declare no conflicts of interest.

References

1. Li, Z.L.; Wu, H.; Duan, S.; Zhao, W.; Ren, H.; Liu, X.; Leng, P.; Tang, R.; Ye, X.; Zhu, J.; et al. Satellite Remote Sensing of Global Land Surface Temperature: Definition, Methods, Products, and Applications. *Rev. Geophys.* **2022**, *61*, e2022RG000777. [CrossRef]
2. Martins, J.; Trigo, I.; Bento, V.; DaCamara, C. A Physically Constrained Calibration Database for Land Surface Temperature Using Infrared Retrieval Algorithms. *Remote Sens.* **2016**, *8*, 808. [CrossRef]
3. Duan, S.B.; Li, Z.L.; Leng, P.J.R.S.o.E. A framework for the retrieval of all-weather land surface temperature at a high spatial resolution from polar-orbiting thermal infrared and passive microwave data. *Remote Sens. Environ.* **2017**, *195*, 107–117. [CrossRef]
4. Firozjaei, M.K.; Kiavarz, M.; Alavipanah, S.K.J.B. Impact of surface characteristics and their adjacency effects on urban land surface temperature in different seasonal conditions and latitudes. *Build. Environ.* **2022**, *219*, 109145. [CrossRef]
5. Zhong, X.; Zhao, L.; Zhang, X.; Wang, J.; Zhao, H.; Ren, P. Analysis of the adjacency effect on retrieval of land surface temperatures based on multimodal images from unmanned aerial vehicles. *Urban Clim.* **2023**, *51*, 101664. [CrossRef]
6. Lai, J.; Zhan, W.; Huang, F.; Quan, J.; Hu, L.; Gao, L.; Ju, W. Does quality control matter? Surface urban heat island intensity variations estimated by satellite-derived land surface temperature products. *ISPRS J. Photogramm. Remote Sens.* **2018**, *139*, 212–227. [CrossRef]
7. Weng, Q. Thermal infrared remote sensing for urban climate and environmental studies: Methods, applications, and trends. *ISPRS J. Photogramm. Remote Sens.* **2009**, *64*, 335–344. [CrossRef]
8. Cao, B.; Gastellu-Etchegorry, J.; Yin, T.; Bian, Z.; Bai, J.; Fang, J.-Y.; Qin, B.; Du, Y.; Li, H.; Xiao, Q.; et al. Optimizing the Protocol of Near-Surface Remote Sensing Experiments Over Heterogeneous Canopy Using DART Simulated Images. *IEEE Trans. Geosci. Remote Sens.* **2023**, *61*, 5000616. [CrossRef]
9. Wan, Z.; Dozier, J.J.I.T.o.G.; Sensing, R. A generalized split-window algorithm for retrieving land-surface temperature from space. *IEEE Trans. Geosci. Remote Sens.* **1996**, *34*, 892–905.
10. Yang, J.; Wong, M.S.; Menenti, M.; Nichol, J.; Sensing, R. Study of the geometry effect on land surface temperature retrieval in urban environment. *ISPRS J. Photogramm. Remote Sens.* **2015**, *109*, 77–87. [CrossRef]
11. Chen, S.; Ren, H.; Ye, X.; Dong, J.; Zheng, Y. Geometry and adjacency effects in urban land surface temperature retrieval from high-spatial-resolution thermal infrared images. *Remote Sens. Environ.* **2021**, *262*, 112518. [CrossRef]
12. Jimenez-Munoz, J.C.; Sobrino, J.A. A Single-Channel Algorithm for Land-Surface Temperature Retrieval from ASTER Data. *IEEE Geosci. Remote Sens. Lett.* **2010**, *7*, 176–179. [CrossRef]
13. Rongali, G.; Keshari, A.K.; Gosain, A.K.; Khosa, R. Split-Window Algorithm for Retrieval of Land Surface Temperature Using Landsat 8 Thermal Infrared Data. *J. Geovisualization Spat. Anal.* **2018**, *2*, 14. [CrossRef]
14. Li, Z.-L.; Tang, B.-H.; Wu, H.; Ren, H.; Yan, G.; Wan, Z.; Trigo, I.F.; Sobrino, J.A. Satellite-derived land surface temperature: Current status and perspectives. *Remote Sens. Environ.* **2013**, *131*, 14–37. [CrossRef]
15. Ru, C.; Duan, S.-B.; Jiang, X.-G.; Li, Z.-L.; Huang, C.; Liu, M. An extended SW-TES algorithm for land surface temperature and emissivity retrieval from ECOSTRESS thermal infrared data over urban areas. *Remote Sens. Environ.* **2023**, *290*, 113544. [CrossRef]
16. Zhen, Z.; Chen, S.; Yin, T.; Gastellu-Etchegorry, J.P. Spatial Resolution Requirements for the Application of Temperature and Emissivity Separation (TES) Algorithm Over Urban Areas. *IEEE J. Sel. Top. Appl. Earth Obs. Remote Sens.* **2022**, *15*, 8990–9003. [CrossRef]
17. Gastellu-Etchegorry, J.-P.; Yin, T.; Lauret, N.; Cajgfinger, T.; Gregoire, T.; Grau, E.; Feret, J.-B.; Lopes, M.; Guilleux, J.; Dedieu, G.; et al. Discrete Anisotropic Radiative Transfer (DART 5) for Modeling Airborne and Satellite Spectroradiometer and LIDAR Acquisitions of Natural and Urban Landscapes. *Remote Sens.* **2015**, *7*, 1667–1701. [CrossRef]
18. Gastellu-Etchegorry, J.P.; Lauret, N.; Yin, T.; Landier, L.; Kallel, A.; Malenovský, Z.; Bitar, A.A.; Aval, J.; Benhmida, S.; Qi, J.; et al. DART: Recent Advances in Remote Sensing Data Modeling With Atmosphere, Polarization, and Chlorophyll Fluorescence. *IEEE J. Sel. Top. Appl. Earth Obs. Remote Sens.* **2017**, *10*, 2640–2649. [CrossRef]
19. Wang, S.; Longhua, H. *Retrieving Land Surface Temperature from MODIS Data Using an Optimized Split-Window Algorithm*; National Natural Science Foundation of China: Beijing, China, 2014.
20. Watson, I.D.; Johnson, G.T. Graphical estimation of sky view-factors in urban environments. *J. Climatol.* **1987**, *7*, 193–197. [CrossRef]
21. Blennow, K. Sky View Factors from High-Resolution Scanned Fish-eye Lens Photographic Negatives. *J. Atmos. Ocean. Technol.* **1995**, *12*, 1357–1362. [CrossRef]
22. Li, J.; Li, K.; Qian, Y.; Dou, X.; Han, Q.; Zeng, J.; Zhao, H.; Lan, Q.; Xu, Z.; Bai, J.; et al. An urban land surface temperature and emissivity separation algorithm from ASTER TIR data and its application. *Int. J. Digit. Earth* **2025**, *18*, 2459346. [CrossRef]
23. Zakšek, K.; Oštir, K.; Kokalj, Ž. Sky-View Factor as a Relief Visualization Technique. *Remote Sens.* **2011**, *3*, 398–415. [CrossRef]
24. Kokalj, Ž.; Zaksek, K.; Oštir, K.; Pehani, P.; Čotar, K.; Somrak, M. *Relief Visualization Toolbox, Version 2.2.1 Manual*; Research Centre of the Slovenian Academy of Sciences and Arts (ZRC SAZU): Ljubljana, Slovenia, 2019.

25. Wang, Y.; Gastellu-Etchegorry, J.-P. DART: Improvement of thermal infrared radiative transfer modelling for simulating top of atmosphere radiance. *Remote Sens. Environ.* **2020**, *251*, 112082. [CrossRef]
26. Kotthaus, S.; Smith, T.E.L.; Wooster, M.J.; Grimmond, C.S.B. Derivation of an urban materials spectral library through emittance and reflectance spectroscopy. *ISPRS J. Photogramm. Remote Sens.* **2014**, *94*, 194–212. [CrossRef]
27. Kotthaus, S.; Smith, T.; Wooster, M.; Grimmond, S. *Spectral Library of Impervious Urban Materials (1.0)*; Zenodo: Geneva, Switzerland, 2013. [CrossRef]
28. Zhang, Q.; Wang, D.; Gastellu-Etchegorry, J.; Yang, J.; Qian, Y. Impact of 3-D structures on directional effective emissivity in urban areas based on DART model. *Build. Environ.* **2023**, *239*, 110410. [CrossRef]
29. Chen, S.; Chen, L.; Ren, H.; Li, Y.; Chen, Y.; Guo, J.; Sun, Y.; Zheng, Y. Quantifying adjacent thermal effects: An essential consideration in evaluating thermal effects of 3-D urban landscapes. *Sustain. Cities Soc.* **2025**, *128*, 106493. [CrossRef]
30. Lagouarde, J.P.; Hénon, A.; Irvine, M.; Voogt, J.; Pigeon, G.; Moreau, P.; Masson, V.; Mestayer, P. Experimental characterization and modelling of the nighttime directional anisotropy of thermal infrared measurements over an urban area: Case study of Toulouse (France). *Remote Sens. Environ.* **2012**, *117*, 19–33. [CrossRef]
31. Widlowski, J.-L.; Taberner, M.; Pinty, B.; Bruniquel-Pinel, V.; Disney, M.; Fernandes, R.A.; Gastellu-Etchegorry, J.P.; Gobron, N.; Kuusk, A.; Lavergne, T.; et al. Third Radiation Transfer Model Intercomparison (RAMI) exercise: Documenting progress in canopy reflectance models. *J. Geophys. Res. Atmos.* **2007**, *112*, D09111. [CrossRef]
32. Sobrino, J.A.; Mattar, C.; Gastellu-Etchegorry, J.P.; Jiménez-Muñoz, J.C.; Grau, E. Evaluation of the DART 3D model in the thermal domain using satellite/airborne imagery and ground-based measurements. *Int. J. Remote Sens.* **2011**, *32*, 7453–7477. [CrossRef]